Research Article

Nano Research
2019, 12(12): 2960–2965

ISSN 1998-0124 CN 11-5974/O4
https://doi.org/10.1007/s12274-019-2538-x

Rational design of phosphorus-doped cobalt sulfides electrocatalysts for hydrogen evolution

Guoxing Qu[1], Tianli Wu[2], Yanan Yu[1], Zekang Wang[1], Yang Zhou[1], Zhendong Tang[3], and Qin Yue[1] (✉)

[1] *Institute of Fundamental and Frontier Sciences, University of Electronic Science and Technology of China, Chengdu 610054, China*
[2] *Henan Key Laboratory of Photovoltaic Materials, Henan University, Kaifeng 475004, China*
[3] *Ordnance NCO Academy, Army Engineering University of PLA, Wuhan 430075, China*

Received: 2 August 2019 / **Revised:** 5 September 2019 / **Accepted:** 7 October 2019

ABSTRACT

Moderate anionic doping is an effective approach to improve the performance of electrocatalysts toward hydrogen evolution reaction (HER) since it can adjust the electronic structure, active site, and phase. The reported studies mainly focus on designing P doped CoS_2, while other phases of cobalt sulfide, such as $Co_{1-x}S$ and Co_9S_8 doped with P are rarely investigated for HER electrocatalysts. Herein, various cobalt sulfides (including $CoS_2/Co_{1-x}S$, $Co_{1-x}S$, and Co_9S_8) doped with P are anchored on carbon cloth through a facile hydrothermal method. Among tested electrocatalysts, P doped $Co_{1-x}S$ exhibits excellent electrocatalytic performance with an overpotential of 110 and 165 mV (vs. RHE) for current densities of 10 and 100 mA·cm^{-2}, respectively. Density functional theory calculations reveal that P doped $Co_{1-x}S$ possesses a smaller bandgap and more optimal hydrogen adsorption sites than pristine $Co_{1-x}S$. This work initially investigates various cobalt sulfides doped with P and further gets insight into the activity improvement mechanism of P doping, which could guide the design of earth-abundant HER electrocatalysts for the "hydrogen economy".

KEYWORDS

hydrogen evolution reaction, electrocatalysts, water splitting, P doping, cobalt sulfide

1 Introduction

Developing clean and renewable energy is significant and urgently demanded since it can alleviate energy crisis and contribute to ecological improvement [1, 2]. Hydrogen is considered as the most promising candidate of ideal energy carriers due to its carbon-free nature, high calorific value, and abundant resource of water [3]. Electrocatalytic water splitting is a green and feasible pathway to generate high-purity molecular hydrogen through the cathodic hydrogen evolution reaction (HER) [4]. However, the application HER process is usually limited by either high cost and scarcity of platinum group metal (PGM) electrocatalysts, or the low efficiency of non-PGM electrocatalysts due to the large overpotential [5, 6]. As a result, efficient and robust non-PGM electrocatalysts are desirable to address the issues of cost and overpotential [7–10].

Transition-metal (Fe, Co, Ni, Mo, W) sulfides and phosphides have attracted extensive attention in the past decades owing to their relatively high electrocatalytic activity and stability compared to other earth-abundant electrocatalysts [8, 11–13]. Various strategies including hybridization [14], defect engineering [15], dimensional control [13], and doping [12, 16], have been developed to further improve the electrocatalytic performances of the sulfides and phosphides. Moderate anionic doping, including phosphorus, sulfur, selenium, carbon, and nitrogen, can effectively improve the HER performances of catalysts [16–19]. Among these, phosphorus-doped metal sulfides are particularly interesting, as P atom has similar atomic radius and electronegativity to S atom, which makes P atom readily dope into sulfides by substituting S atom and bonding with the metal atom, and then trigger lattice distortion [20, 21]. Such a slight change in their mother lattice structure may provide new active sites, optimize hydrogen adsorption energy, or/and modulate electronic band structures, which might be beneficial to improving electrocatalytic performance [22]. Jin et al. established ternary pyrite-type cobalt phosphosulphide (CoPS) as a high-performance HER electrocatalyst by both theoretical and experimental study [23]. Ouyang et al. prepared phosphorus-doped cobalt disulfide nanosheet electrocatalyst and demonstrated that P doping significantly improved its electrocatalytic performance [24]. Wang and coworkers synthesized ternary cobalt phosphosulfide (CoS|P) nanoparticle electrocatalysts anchored on carbon nanotubes with enhanced electrocatalytic activity and stability [21]. Gao's group has systematically studied the effect of P dopant content on the electrocatalytic performance of CoS_2 [22]. Despite a few studies have focused on CoS_2 phase doped with P, other cobalt sulfides including $Co_{1-x}S$ and Co_9S_8 phases incorporated with P have rarely been systematically investigated for HER catalysis. Considering various crystalline phase can effectively influence the electrocatalytic activity, it is necessary to design various cobalt sulfides with P doping and systematically investigate their HER performances.

Herein, we report a universal synthesis of various cobalt sulfides doped with P, involving $CoS_2/Co_{1-x}S$, $Co_{1-x}S$ and Co_9S_8 phase. These P doped electrocatalysts anchored on the fibers of carbon cloth are prepared through a facile one-pot hydrothermal method. It is found that hydrothermal temperature has a crucial influence on the phase of final products. The electrocatalytic HER performances of these P doped cobalt sulfides are investigated. P doped hexagonal $Co_{1-x}S$ shows the highest electrocatalytic activity with a η_{10} (η_x: the overpotential required to provide a current density of x mA·cm^{-2}) of 110 mV,

Address correspondence to qinyue@uestc.edu.cn

much lower than 180 mV for pristine $Co_{1-x}S$. It demonstrates that the introduction of P can effectively enhance the HER activity of P doped $Co_{1-x}S$. Theoretical calculations further confirm that P doping can improve conductivity, optimize hydrogen adsorption energy, and thus enhance the intrinsic activity of P doped $Co_{1-x}S$.

2 Experimental section

2.1 Synthesis of P doped cobalt sulfides

All the samples were synthesized through a facile one-pot segmented hydrothermal method. To start with, three pieces of hydrophilic carbon cloth with an area of 1 cm × 1.5 cm were cleaned by ultrasonication in absolute ethanol and deionized water in turn before use. Then, 0.163 g of cobalt chloride ($CoCl_2$), 0.074 g of ammonium fluoride (NH_4F) and 0.31 g of sodium thiosulfate pentahydrate ($Na_2S_2O_3{\cdot}5H_2O$,) were dissolved into 30 mL of deionized water and the mixture was continually stirred for two hours at room temperature. Then the cleaned carbon cloths were put into the mixed solution followed by adding 0.879 g of sodium hypophosphite (NaH_2PO_2) into the mixture and stirring until dissolved. After that, the precursor mixture was transferred into 100 mL Teflon-lined stainless autoclave. The hydrothermal process was set as two segments. All the samples firstly reacted at 105 °C for 5 h and then were further heated to 160, 180, and 200 °C, respectively, for another 30 h. The final carbon cloth coated with P doped cobalt sulfides was taken out after cooling down, washed with deionized water and then directly used as self-supported cathode after natural drying.

2.2 Electrocatalytic measurements

All the electrochemical tests were conducted in a standard three-electrode setup by an electrochemistry workstation (CHI 760E, CH Instruments, USA) with 0.5 M H_2SO_4 solution as the electrolyte. The as-prepared carbon cloth electrodes, a Pt sheet and a saturated calomel electrode (SCE) were used as the working electrodes, the counter electrode, and the reference electrode, respectively. The reference electrode was calibrated with reversible hydrogen electrode (RHE) prior to measurement, yielding an equation of $E_{(RHE)} = E_{(SCE)} + 279$ mV. The linear sweep voltamperometry (LSV) was scanned at a rate of 5 mV·s^{-1}. Electrochemical impedance spectroscopy (EIS) was performed at an overpotential of 50 mV and an amplitude of 5 mV in a frequency range of 100 kHz to 100 MHz. The chronopotentiometry test was carried out at the overpotential to achieve 10 mA·cm^{-2}. All the potentials reported here were versus RHE, and all LSV curves were corrected for an ohmic drop according to the equation $E_{Corrected} = E_{Raw} - IR_s$ (R_s is the equivalent series resistance derived from EIS).

2.3 Physical characterizations

The phase composition was characterized by an X-ray diffractometer (D/max-2400, Rigaku, Japan) using Cu Kα (K = 1.54 Å) radiation in the 2θ range of 3°–80°. Morphologies and element mapping were characterized by a field-emission scanning electron microscope (S-4700, Hitachi, Japan) equipped with energy-dispersive X-ray spectroscopy (EDX). Elements quantitative analysis was conducted on inductively coupled plasma-optical emission spectrometer (ICP-OES, ICPOES730, Agilent, China). Granule structure and crystal determination were analyzed by a transmission electron microscope (Libra 200 FE, Carl Zeiss, Germany). Elementary composition and chemical valence states were analyzed by X-ray photoelectron spectrometer (VGESCALAB MK II, VG, UK) with Mg Kα as the excitation source.

3 Results and discussion

The preparation procedures of P doped cobalt sulfides are schematically illustrated in Fig. 1(a). The required amount of cobalt chloride, ammonium fluoride, and sodium thiosulfate is mixed and dissolved in deionized water to form a clear pinkish solution. Then sodium hypophosphite and three pieces of hydrophilic carbon cloth are added into the pinkish solution as a phosphorus source and deposition carrier, respectively. The final mixtures are transferred into stainless autoclaves to execute segmented hydrothermal programs of holding temperature at 105 °C for 5 h and followed by holding at 160, 180 and 200 °C for another 30 h, generating different samples. The first temperature step at 105 °C can facilitate the homogeneous nucleation precursors.

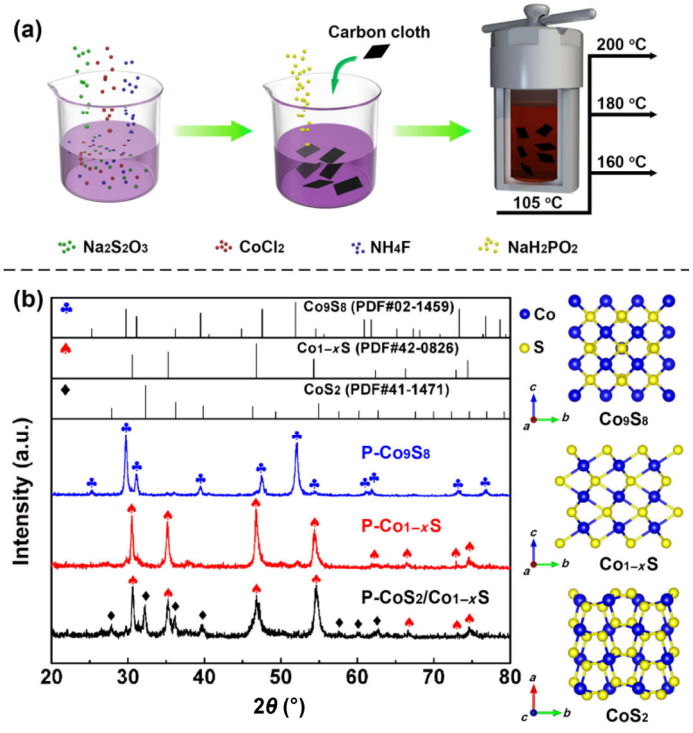

Figure 1 (a) Schematic illustration for synthetic procedures of P-Co_9S_8, P-$Co_{1-x}S$ and P-CoS_2/$Co_{1-x}S$. (b) XRD patterns of P-Co_9S_8, P-$Co_{1-x}S$ and P-CoS_2/$Co_{1-x}S$. The standard XRD patterns and the crystal structure of Co_9S_8, $Co_{1-x}S$ and CoS_2 are given for reference.

Wide-angle X-ray diffraction (XRD) measurements are employed to analyze the phase composition of the obtained samples. As shown in Fig. 1(b), it demonstrates that hydrothermal temperature has a crucial influence on the phase of final products. The sample hydrothermal treated at 200 °C and 180 °C is mainly composed of cubic Co_9S_8 (PDF#02-1459) and hexagonal $Co_{1-x}S$ (PDF#42-0826) phase, respectively. However, that obtained under 160 °C contains two primary phases of cubic CoS_2 (PDF#41-1471) and $Co_{1-x}S$, with mass fractions of 46.9% and 53.1%, respectively, obtained through quantitative analysis from XRD profile-fitted peaks as shown in Fig. S1 in the Electronic Supplementary Material (ESM). From the crystal structure diagrams shown in Fig. 1(b), Co_9S_8, $Co_{1-x}S$, and CoS_2 is assigned to the space group of $Fm\bar{3}m$, $P6_3/mmc$, and $Pa\bar{3}$, respectively. For convenience, the P doped cobalt sulfides obtained at the hydrothermal temperature of 160, 180, and 200 °C are denoted as P-CoS_2/$Co_{1-x}S$, P-$Co_{1-x}S$, and P-Co_9S_8, respectively.

Figures 2(a)–2(c) show the full view scanning electron microscopy (SEM) images of P-Co_9S_8, P-$Co_{1-x}S$, and P-CoS_2/$Co_{1-x}S$, respectively. No agglomeration blocks are observed, indicating a uniform deposition of cobalt sulfides on the carbon cloth. The corresponding local view SEM images (Figs. 2(d)–2(f)) exhibit that all the fibers of carbon cloth are uniformly covered with particles of cobalt sulfides. The enlarged SEM images (Figs. 2(d)–2(f), insets) reveal these rough particles contain an aggregation of small primary particles and possess an integrated particle size of ~ 3 μm. EDX mapping is conducted to display the distribution of elements in the particles. As shown in

Figs. 2(g)–2(i), Co, S and P elements are uniformly distributed throughout the entire particles. The corresponding EDX spectra in Fig. S2 in the ESM further confirm the existence of P element in P-CoS_2/$Co_{1-x}S$, P-$Co_{1-x}S$, and P-Co_9S_8. ICP-OES test (Fig. S3 in the ESM) shows that the atomic percentage of P in P-CoS_2/$Co_{1-x}S$, P-$Co_{1-x}S$ and P-Co_9S_8 is 1.8%, 5.6% and 1.7%, respectively. Combined with XRD analysis that no phosphide is detected, it can be speculated that P elements are doped into the cobalt sulfides.

X-ray photoelectron spectroscopy (XPS) spectra are recorded to verify the composition and valence of the samples. Figure 3(a) shows the full-survey XPS spectra from 100 to 800 eV of P-Co_9S_8, P-$Co_{1-x}S$, and P-CoS_2/$Co_{1-x}S$. It reveals the existence of Co, O, C, S, and P elements, where C element is originated from the carbon cloth substrate and the calibrated carbon, and O element is derived from the slight surface oxidization of metal and adsorbed oxygen. The remaining Co, S, and P stem from the particles of P doped cobalt sulfides, in accordance with the EDX characterization above. Figure 3(b) shows the high-resolution profiles of S 2p for P-CoS_2/$Co_{1-x}S$, P-$Co_{1-x}S$, and P-Co_9S_8. The peaks located at higher than 166.0 eV without deconvolution are assigned to S–O species resulting from surface oxidization [24]. The doublets near 163.8 and 161.5 eV can be assigned to the S $2p_{1/2}$ and S $2p_{3/2}$ for S–Co species [25]. Compared

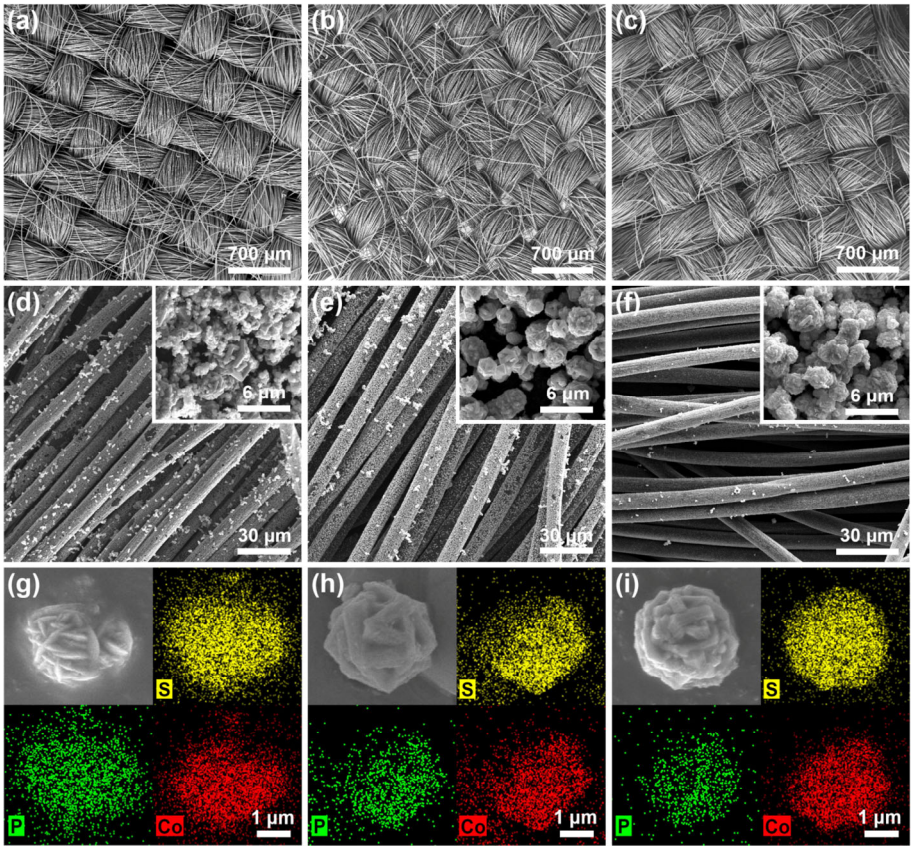

Figure 2 SEM images of ((a) and (d)) P-CoS_2/$Co_{1-x}S$, ((b) and (e)) P-$Co_{1-x}S$, and ((c) and (f)) P-Co_9S_8. The insets are the SEM images of the corresponding particles of HER active species. Element mapping of the particles of (g) P-CoS_2/$Co_{1-x}S$, (h) P-$Co_{1-x}S$ and (i) P-Co_9S_8.

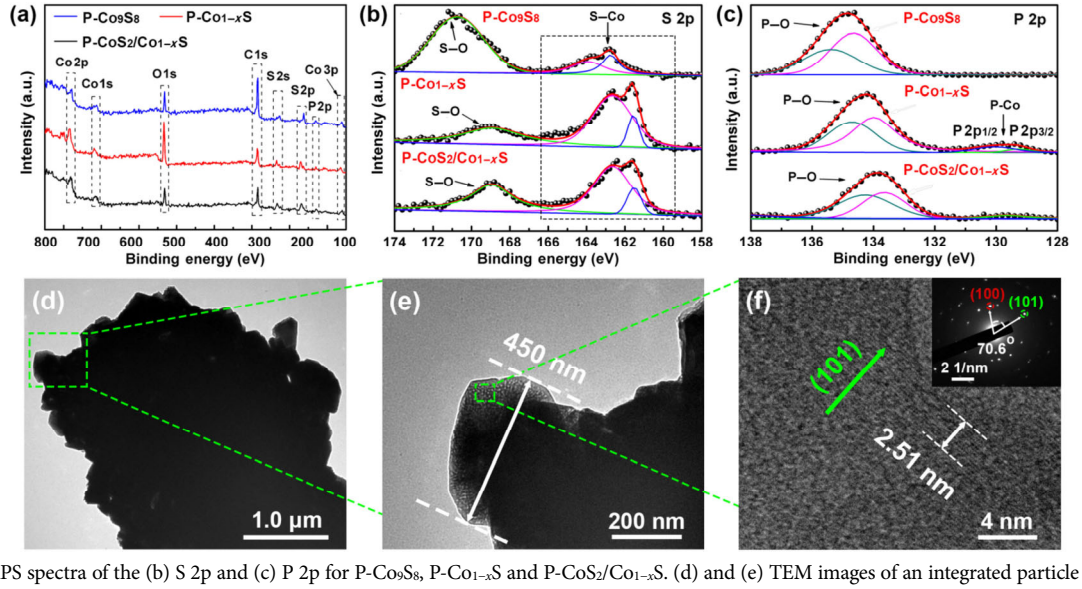

Figure 3 (a)–(c) XPS spectra of the (b) S 2p and (c) P 2p for P-Co_9S_8, P-$Co_{1-x}S$ and P-CoS_2/$Co_{1-x}S$. (d) and (e) TEM images of an integrated particle of P-$Co_{1-x}S$. (f) The high-resolution TEM image of P-$Co_{1-x}S$ (inset: corresponding selected-area electron diffraction pattern).

with P-Co_9S_8, P-$Co_{1-x}S$ and P-$CoS_2/Co_{1-x}S$ exhibit stronger low-energy peaks regarding the S–Co species, and weaker high-energy peaks regarding S–O species, implying a higher S-Co species density in P-$Co_{1-x}S$ and P-$CoS_2/Co_{1-x}S$. The high-resolution P 2p profiles (Fig. 3(c)) for these samples exhibit distinct doublets higher than 132 eV which should be assigned to high valence P in P–O species [26]. All the samples of P-Co_9S_8, P-$Co_{1-x}S$ and P-$CoS_2/Co_{1-x}S$ show strong peaks regarding P–O species. This is because P elements on the surface are easily oxidized and such phenomenon is very common in P-containing composites [27]. Moreover, the binding energy of P–O band shows clearly positive shift for P-$CoS_2/Co_{1-x}S$, P-$Co_{1-x}S$ and P-Co_9S_8, indicating an increased degree of P oxidation with the increased hydrothermal temperature. Even so, the doublets between 131 and 128 eV attributed to the P $2p_{1/2}$ and P $2p_{3/2}$ peaks of P-Co species can be expressly detected for P-$Co_{1-x}S$, indicating the distinct high P-Co species density in this sample. The peaks of P-Co species are also visible in the enlarged P 2p profile of P-$CoS_2/Co_{1-x}S$, as shown in Fig. S4 in the ESM. No distinct P-Co peak is visible for P-Co_9S_8 due to the low P content (atom ratio of 1.7%) determined by ICP-OES and easy to oxidation by air on the surface [27]. The high-resolution Co 2p spectra of P-$CoS_2/Co_{1-x}S$, P-$Co_{1-x}S$, and P-Co_9S_8 are displayed in Figs. S5(a)–S5(c) in the ESM, respectively. The peaks at about 778.9 eV can be ascribed to Co $2p_{3/2}$ for Co-S species [28]. The doublets between 790.0 and 780.0 eV are assigned to the Co-O species [24], due to that cobalt sulfides are susceptible to oxidation upon exposure to air. Furthermore, P-$Co_{1-x}S$ and P-$CoS_2/Co_{1-x}S$ exhibit much stronger peaks regarding Co-S species than P-Co_9S_8, coinciding with the profile of S 2p.

Transmission electron microscopy (TEM) is employed to further investigate the granule structure of P-$Co_{1-x}S$. As shown in Figs. 3(d) and 3(e), the particle from P-$Co_{1-x}S$ comprises of many aggregated small particles with a size of ~ 450 nm. The high-resolution TEM (HRTEM) image in Fig. 3(f) displays a clear lattice fringe spacing of 0.251 nm, which could be indexed to (101) crystal facet of hexagonal $Co_{1-x}S$. The selected area electron diffraction (SAED) illustrates a spotted pattern corresponding to the diffraction lattice faces of (100) and (110) along the [010] zone axis of $Co_{1-x}S$ hexagonal structure (the inset in Fig. 3(f)), indicating the high purity of $Co_{1-x}S$ hexagonal phase in P-$Co_{1-x}S$.

Electrochemical tests are carried out in a three-electrode cell setup using N_2-saturated 0.5 M H_2SO_4 aqueous solution as the electrolyte. To remove impurities and stabilize catalysts, all the cathodes are cycled 10 times of CV between −0.3 and 0.2 V vs. RHE at a scan rate of 20 mV·s^{-1} before recording data. Figure 4(a) presents the LSV curves of P-Co_9S_8, P-$Co_{1-x}S$, P-$CoS_2/Co_{1-x}S$, bare carbon cloth, and Pt sheet. Pt sheet shows superexcellent HER performance, while bare carbon cloth exhibits a negligible HER activity. Sample P-$Co_{1-x}S$ requires an overpotential of 110 mV to achieve a current density of 10 mA·cm^{-2}, smaller than that of P-$CoS_2/Co_{1-x}S$ (η_{10} = 129 mV) and P-Co_9S_8 (η_{10} of 161 mV). To provide a high cathodic current density of 100 mA·cm^{-2}, P-$Co_{1-x}S$ requires a η_{100} of only 165 mV, much smaller than 230 mV for P-$CoS_2/Co_{1-x}S$ and 270 mV for P-Co_9S_8. To investigate the advantages of P doping, the corresponding undoped samples are also synthesized in the same procedure in the absence of sodium hypophosphite. Figure S6 in the ESM shows the XRD patterns of the undoped samples, indicating almost the same crystal phase with their P doped ones. The LSV curves of $CoS_2/Co_{1-x}S$, $Co_{1-x}S$ and Co_9S_8 are shown in Fig. S7 in the ESM. It can be seen that all the undoped samples show obviously inferior HER activity compared with their doped counterpart. $Co_{1-x}S$ exhibits the highest catalytic activity among these undoped samples, in accordance with previous report that Co(II) coordinated with sulfide has highly efficient activity for catalytic hydrogen evolution [29, 30]. Figure 4(b) reveals the Nyquist plots and the corresponding fitting curves of P-Co_9S_8, P-$Co_{1-x}S$, and P-$CoS_2/Co_{1-x}S$. The inset is the fitting circuit diagram which consists

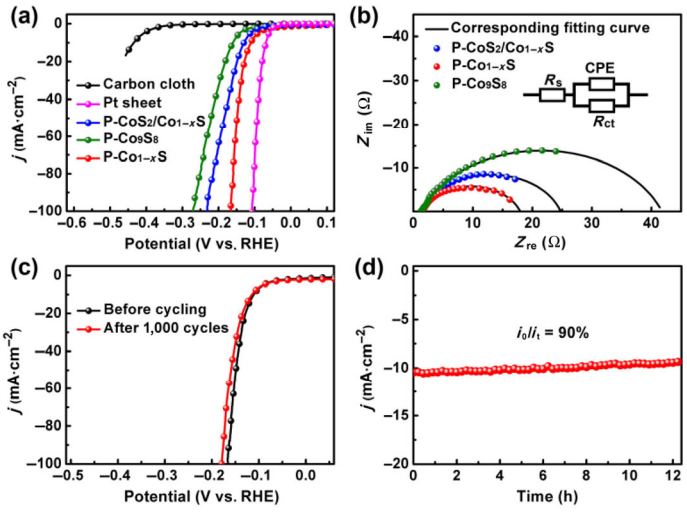

Figure 4 (a) LSV curves of bare carbon cloth, P-Co_9S_8, P-$Co_{1-x}S$, P-$CoS_2/Co_{1-x}S$ and Pt sheet. (b) Nyquist plots of P-Co_9S_8, P-$Co_{1-x}S$ and P-$CoS_2/Co_{1-x}S$ (inset: fitting circuit diagram for tested EIS). (c) Stability test of P-$Co_{1-x}S$ electrode by showing the LSV curves before and after 1,000 cycles. (d) Chronopotentiometry curve for P-$Co_{1-x}S$.

of a series of resistance (R_s), a charge transfer resistance (R_{ct}) and a constant phase element (CPE). Similar small R_s (< 2 Ω) is generated for all the samples, indicating the particles of the P doped cobalt sulfides are tightly anchored on carbon cloth [19]. The semicircle in the Nyquist plots is associated with the process of charge transfer to the electrode from solution and the diameter of the semicircle along the *X*-axis represents the value of R_{ct}, reflecting the kinetic rate of HER [31]. As shown in Fig. 4(b), P-$Co_{1-x}S$ exhibits much smaller R_{ct} of 16.4 Ω·cm^2 compared to 23.2 Ω·cm^2 for P-$CoS_2/Co_{1-x}S$ and 40.1 Ω·cm^2 for P-Co_9S_8, demonstrating the fastest electron transfer rates and HER kinetics of P-$Co_{1-x}S$ [32]. As discussed above, P-$Co_{1-x}S$ with the highest Co-P species and Co-S density exhibits superior electrocatalytic HER activity to P-Co_9S_8 and P-$CoS_2/Co_{1-x}S$ which possess much lower Co-P species density. Thus it is speculated that Co-P and Co-S species have a promotion effect on the active catalytic site for these P doped cobalt sulfides. Operational durability is another important criterion for HER electrocatalysts. To assess the long-term cycling stability, P-$Co_{1-x}S$ is carried out 1,000 times of cyclic voltammetry (CV) between −0.2 and 0.2 V (vs. RHE) at a scan rate of 100 mV·s^{-1}. Figure 4(c) reveals the LSV curves before and after cycling. The activity exhibits slight degradation with an overpotential increase of merely 14 mV at 100 mA·cm^{-2}. In addition, the long-term electrocatalytic stability of P-$Co_{1-x}S$ is also tested by chronopotentiometry. As shown in Fig. 4(d), the cathodic current decreases slowly with a high retention rate of ~ 90% after more than 12 h running, suggesting excellent stability in long-term catalyzing HER for P-$Co_{1-x}S$ in acidic media.

Since P-$Co_{1-x}S$ and pristine $Co_{1-x}S$ exhibit the highest HER activity among the three P-doped cobalt sulfides and the three undoped samples, respectively. The counterparts of P-doped $Co_{1-x}S$ and pristine $Co_{1-x}S$ are chosen to further investigate the effect of phosphorus doping on the HER activity. EDX spectrum in Fig. S2(d) in the ESM shows the presence of Co and S elements, without obvious P elements in pristine $Co_{1-x}S$. The XRD pattern (Fig. S6 in the ESM) confirms that pristine $Co_{1-x}S$ possess similar distinct diffraction peaks indexed to hexagonal phase $Co_{1-x}S$, in accordance with P-$Co_{1-x}S$. SEM images (Fig. S8 in the ESM) demonstrate that the particles of pristine $Co_{1-x}S$ with rough surface morphology are uniformly and tightly anchored on carbon cloth, similar to the P doped $Co_{1-x}S$ particles of P-$Co_{1-x}S$. The similar structure and morphology enable a systematic and fair study for investigating the effect of phosphorus doping on HER activity. The HER performances of pristine $Co_{1-x}S$ and P-$Co_{1-x}S$ are

compared. As shown in Fig. S9 in the ESM, pristine $Co_{1-x}S$ is much inferior to P-$Co_{1-x}S$ in terms of electrocatalytic HER activity with much higher η_{10} of 180 mV (vs. 110 mV for P-$Co_{1-x}S$), η_{100} of 247 mV (vs. 165 mV for P-$Co_{1-x}S$). As a result, it is believed the doped P elements play a crucial role in the improved electrocatalytic HER activity for P-$Co_{1-x}S$.

To understand the mechanism of phosphorus doping for HER activity improvements, density functional theory (DFT) simulations are carried out to investigate the hydrogen adsorption Gibbs free energy and electronic band structures. It is proposed that HER performance of electrocatalyst is strongly correlated with the atomic hydrogen adsorption Gibbs free energy (ΔG_{H^*}) on the surface of the electrocatalyst. An ideal ΔG_{H^*} should be close to 0 eV, because intermediate binding energies lead to a balance between the rate of proton reduction and the ease of adsorbed hydrogen from the surface [33]. According to the exposed stable crystal face characterized by TEM and P doing content tested by ICP-OES, adsorbed H* on the (101) lattice face of $Co_{1-x}S$ and P doped $Co_{1-x}S$ with P doing content of 6% are established to study their ΔG_{H^*} as shown in Fig. 5(a). The ΔG_{H^*} at the Co sites of P doped $Co_{1-x}S$ (+0.31 eV) reveals a slight decrease compared to that of pure $Co_{1-x}S$ (+0.59 eV), implying the faster hydrogen adsorption and proton reduction on P doped $Co_{1-x}S$ (Fig. 5(b)). However, the P sites of the sample exhibit a ΔG_{H^*} of −0.29 eV, indicating the P sites with high electronegativity are inclined to adsorb hydrogen. As a result, ΔG_{H^*} at the adjacent Co site further decreases to +0.22 eV. The calculated electron bands of $Co_{1-x}S$ and P doped $Co_{1-x}S$ are shown in Fig. 5(c). $Co_{1-x}S$ possesses a wide band-gap of about 1.58 eV, consistent with the reported value [34]. However, the band-gap decreases to 1.22 eV after P doping, indicating that P doped $Co_{1-x}S$ displays a better electronic conductivity than pristine $Co_{1-x}S$. High conductivity can facilitate electron transfer in the electrocatalytic process [35]. All computational results manifest that P dopants can effectively enhance the HER electrocatalytic activity of P doped $Co_{1-x}S$ through improving the conductivity, promoting hydrogen adsorption and proton reduction by decreasing the bandgap and ΔG_{H^*} of Co sites.

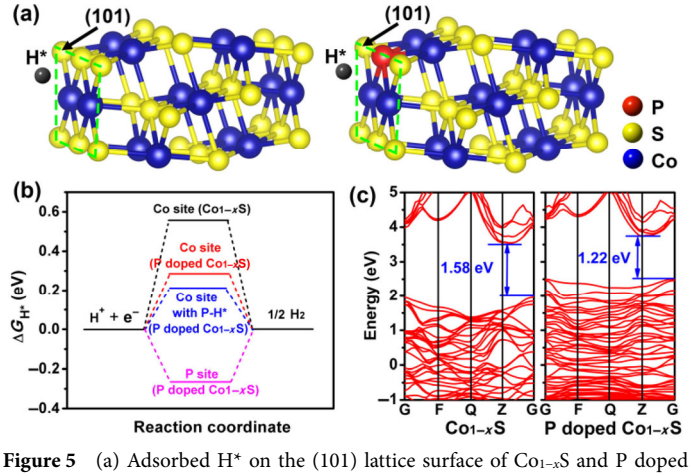

Figure 5 (a) Adsorbed H* on the (101) lattice surface of $Co_{1-x}S$ and P doped $Co_{1-x}S$. (b) The calculated free-energy diagram of the HER on different sites of P doped $Co_{1-x}S$ catalysts. (c) Electronic band structures of pristine $Co_{1-x}S$ and P doped $Co_{1-x}S$.

4 Conclusions

In summary, a facile and universal synthesis of P doped cobalt sulfides with different phases, including CoS_2, $Co_{1-x}S$, and Co_9S_8, are reported. It is found that hydrothermal temperature has a crucial influence on the phases of final products of cobalt sulfides. P doped hexagonal $Co_{1-x}S$ shows excellent electrocatalytic HER performances with a η_{10} of 110 mV, η_{100} of 165 mV and an activity retention of ~ 90% after operating for more than 12 h. Thus P doped $Co_{1-x}S$ is a new promising HER electrocatalysts. Furthermore, DFT calculations imply that P doping can reduce the bandgap of $Co_{1-x}S$ and optimize the ΔG_{H^*} on Co sites, thus enhancing the intrinsic HER activity of P doped $Co_{1-x}S$. This work not only initially investigates different cobalt sulfides doped with P, but also further gets insight into the activity improvement mechanism of P doping, rendering useful guidance for the design of earth-abundant catalyst systems for large scale electrolysis hydrogen production.

Acknowledgements

This work was financially supported by the National Natural Science Foundation of China (No. 21701153) and National Postdoctoral Program for Innovative Talents (No. BX201700042).

Electronic Supplementary Material: Supplementary material (additional information about the theoretical calculations, quantitative analysis, EDX spectra, ICP-OES test result, high resolution XPS spectra, XRD patterns, SEM image, and supporting electrochemical performances) is available in the online version of this article at https://doi.org/10.1007/s12274-019-2538-x.

References

[1] Dresselhaus, M. S.; Thomas, I. L. Alternative energy technologies. *Nature* **2001**, *414*, 332–337.
[2] Liu, J.; Liu, Y.; Liu, N. Y.; Han, Y. Z.; Zhang, X.; Huang, H.; Lifshitz, Y.; Lee, S. T.; Zhong, J.; Kang, Z. H. Metal-free efficient photocatalyst for stable visible water splitting via a two-electron pathway. *Science* **2015**, *347*, 970–974.
[3] Tian, J. Q.; Liu, Q.; Cheng, N. Y.; Asiri, A. M.; Sun, X. P. Self-supported Cu_3P nanowire arrays as an integrated high-performance three-dimensional cathode for generating hydrogen from water. *Angew. Chem., Int. Ed.* **2014**, *53*, 9577–9581.
[4] Turner, J. A. Sustainable hydrogen production. *Science* **2004**, *305*, 972–974.
[5] Nocera, D. G. The artificial leaf. *Acc. Chem. Res.* **2012**, *45*, 767–776.
[6] Subbaraman, R.; Tripkovic, D.; Strmcnik, D.; Chang, K. C.; Uchimura, M.; Paulikas, A. P.; Stamenkovic, V.; Markovic, N. M. Enhancing hydrogen evolution activity in water splitting by tailoring Li^+-$Ni(OH)_2$-Pt interfaces. *Science* **2011**, *334*, 1256–1260.
[7] Kibsgaard, J.; Tsai, C.; Chan, K. R.; Benck, J. D.; Nørskov, J. K.; Abild-Pedersen, F.; Jaramillo, T. F. Designing an improved transition metal phosphide catalyst for hydrogen evolution using experimental and theoretical trends. *Energy Environ. Sci.* **2015**, *8*, 3022–3029.
[8] Wu, T. L.; Pi, M. Y.; Zhang, D. K.; Chen, S. J. 3D structured porous CoP_3 nanoneedle arrays as an efficient bifunctional electrocatalyst for the evolution reaction of hydrogen and oxygen. *J. Mater. Chem. A* **2016**, *4*, 14539–14544.
[9] Liao, L.; Wang, S. N.; Xiao, J. J.; Bian, X. J.; Zhang, Y. H.; Scanlon, M. D.; Hu, X. L.; Tang, Y.; Liu, B. H.; Girault, H. H. A nanoporous molybdenum carbide nanowire as an electrocatalyst for hydrogen evolution reaction. *Energy Environ. Sci.* **2014**, *7*, 387–392.
[10] Wu, T. L.; Dang, Y. L.; He, J. K.; Li, T.; Qu, G. X.; Gao, Y. Y.; Tan, F. R. Synthesis and mechanism investigation of three-dimensional porous CoP_3 nanoplate arrays as efficient hydrogen evolution reaction electrocatalyst. *Appl. Surf. Sci.* **2019**, *494*, 179–186.
[11] Ye, R. Q.; del Angel-Vicente, P.; Liu, Y. Y.; Arellano-Jimenez, M. J.; Peng, Z. W.; Wang, T.; Li, Y. L.; Yakobson, B. I.; Wei, S. H.; Yacaman, M. J. et al. High-performance hydrogen evolution from $MoS_{2(1-x)}P_x$ solid solution. *Adv. Mater.* **2016**, *28*, 1427–1432.
[12] Wang, D. Y.; Gong, M.; Chou, H. L.; Pan, C. J.; Chen, H. A.; Wu, Y. P.; Lin, M. C.; Guan, M. Y.; Yang, J.; Chen, C. W. et al. Highly active and stable hybrid catalyst of cobalt-doped FeS_2 nanosheets-carbon nanotubes for hydrogen evolution reaction. *J. Am. Chem. Soc.* **2015**, *137*, 1587–1592.
[13] Cheng, L.; Huang, W. J.; Gong, Q. F.; Liu, C. H.; Liu, Z.; Li, Y. G.; Dai, H. J. Ultrathin WS_2 nanoflakes as a high-performance electrocatalyst for the hydrogen evolution reaction. *Angew. Chem., Int. Ed.* **2014**, *53*, 7860–7863.
[14] Li, Y. G.; Wang, H. L.; Xie, L. M.; Liang, Y. Y.; Hong, G. S.; Dai, H. J. MoS_2 nanoparticles grown on graphene: An advanced catalyst for the hydrogen evolution reaction. *J. Am. Chem. Soc.* **2011**, *133*, 7296–7299.

[15] Xie, J. F.; Zhang, H.; Li, S.; Wang, R. X.; Sun, X.; Zhou, M.; Zhou, J. F.; Lou, X. W.; Xie, Y. Defect-rich MoS_2 ultrathin nanosheets with additional active edge sites for enhanced electrocatalytic hydrogen evolution. *Adv. Mater*. **2013**, *25*, 5807–5813.

[16] Xie, J. F.; Zhang, J. J.; Li, S.; Grote, F.; Zhang, X. D.; Zhang, H.; Wang, R. X.; Lei, Y.; Pan, B. C.; Xie, Y. Controllable disorder engineering in oxygen-incorporated MoS_2 ultrathin nanosheets for efficient hydrogen evolution. *J. Am. Chem. Soc*. **2013**, *135*, 17881–17888.

[17] Yan, D. F.; Chen, R.; Xiao, Z. H.; Wang, S. Y. Engineering the electronic structure of Co_3O_4 by carbon-doping for efficient overall water splitting. *Electrochim. Acta* **2019**, *303*, 316–322.

[18] Zhang, X. W.; Meng, F.; Mao, S.; Ding, Q.; Shearer, M. J.; Faber, M. S.; Chen, J. H.; Hamers, R. J.; Jin, S. Amorphous MoS_xCl_y electrocatalyst supported by vertical graphene for efficient electrochemical and photoelectrochemical hydrogen generation. *Energy Environ. Sci*. **2015**, *8*, 862–868.

[19] Wang, K.; Zhou, C. J.; Xi, D.; Shi, Z. Q.; He, C.; Xia, H. Y.; Liu, G. W.; Qiao, G. J. Component-controllable synthesis of $Co(S_xSe_{1-x})_2$ nanowires supported by carbon fiber paper as high-performance electrode for hydrogen evolution reaction. *Nano Energy* **2015**, *18*, 1–11.

[20] Brumme, T.; Calandra, M.; Mauri, F. First-principles theory of field-effect doping in transition-metal dichalcogenides: Structural properties, electronic structure, hall coefficient, and electrical conductivity. *Phys. Rev. B* **2015**, *91*, 155436.

[21] Liu, W.; Hu, E. Y.; Jiang, H.; Xiang, Y. J.; Weng, Z.; Li, M.; Fan, Q.; Yu, X. Q.; Altman, E. I.; Wang, H. L. A highly active and stable hydrogen evolution catalyst based on pyrite-structured cobalt phosphosulfide. *Nat. Commun*. **2016**, *7*, 10771.

[22] Zhang, J. Y.; Liu, Y. C.; Xia, B. R.; Sun, C. Q.; Liu, Y. G.; Liu, P. T.; Gao, D. Q. Facile one-step synthesis of phosphorus-doped CoS_2 as efficient electrocatalyst for hydrogen evolution reaction. *Electrochim. Acta* **2018**, *259*, 955–961.

[23] Caban-Acevedo, M.; Stone, M. L.; Schmidt, J. R.; Thomas, J. G.; Ding, Q.; Chang, H. C.; Tsai, M. L.; He, J. H.; Jin, S. Efficient hydrogen evolution catalysis using ternary pyrite-type cobalt phosphosulphide. *Nat. Mater*. **2015**, *14*, 1245–1251.

[24] Ouyang, C. B.; Wang, X.; Wang, S. Y. Phosphorus-doped CoS_2 nanosheet arrays as ultra-efficient electrocatalysts for the hydrogen evolution reaction. *Chem. Commun*. **2015**, *51*, 14160–14163.

[25] Zhu, H.; Zhang, J. F.; Yanzhang, R. P.; Du, M. L.; Wang, Q. F.; Gao, G. H.; Wu, J. D.; Wu, G. M.; Zhang, M.; Liu, B. et al. When cubic cobalt sulfide meets layered molybdenum disulfide: A core-shell system toward synergetic electrocatalytic water splitting. *Adv. Mater*. **2015**, *27*, 4752–4759.

[26] Zhang, R.; Wang, X. X.; Yu, S. J.; Wen, T.; Zhu, X. W.; Yang, F. X.; Sun, X. N.; Wang, X. K.; Hu, W. P. Ternary $NiCo_2P_x$ nanowires as pH-universal electrocatalysts for highly efficient hydrogen evolution reaction. *Adv. Mater*. **2017**, *29*, 1605502.

[27] Wang, T. Y.; Du, K. Z.; Liu, W. L.; Zhu, Z. W.; Shao, Y. H.; Li, M. X. Enhanced electrocatalytic activity of MoP microparticles for hydrogen evolution by grinding and electrochemical activation. *J. Mater. Chem. A* **2015**, *3*, 4368–4373.

[28] Li, J. Y.; Zhou, X. M.; Xia, Z. M.; Zhang, Z. Y.; Li, J.; Ma, Y. Y.; Qu, Y. Q. Facile synthesis of CoX (X = S, P) as an efficient electrocatalyst for hydrogen evolution reaction. *J. Mater. Chem. A* **2015**, *3*, 13066–13071.

[29] Zhao, G. X.; Sun, Y. B.; Zhou, W.; Wang, X. K.; Chang, K.; Liu, G. G.; Liu, H. M.; Kako, T.; Ye, J. H. Superior photocatalytic H_2 production with cocatalytic Co/Ni species anchored on sulfide semiconductor. *Adv. Mater*. **2017**, *29*, 1703258.

[30] Lyu, Y. H.; Wang, R. L.; Tao, L.; Zou, Y. Q.; Zhou, H. J.; Liu, T. T.; Zhou, Y. Y.; Huo, J.; Jiang, S. P.; Zheng, J. Y. et al. *In-situ* evolution of active layers on commercial stainless steel for stable water splitting. *Appl. Catal. B: Environ*. **2019**, *248*, 277–285.

[31] Bao, J.; Zhang, X. D.; Fan, B.; Zhang, J. J.; Zhou, M.; Yang, W. L.; Hu, X.; Wang, H.; Pan, B. C.; Xie, Y. Ultrathin spinel-structured nanosheets rich in oxygen deficiencies for enhanced electrocatalytic water oxidation. *Angew. Chem*. **2015**, *127*, 7507–7512.

[32] Jiang, J.; Gao, M. R.; Sheng, W. C.; Yan, Y. S. Hollow chevrel-phase $NiMo_3S_4$ for hydrogen evolution in alkaline electrolytes. *Angew. Chem*. **2016**, *55*, 15240–15245.

[33] Greeley, J.; Nørskov, J. K. Large-scale, density functional theory-based screening of alloys for hydrogen evolution. *Surf. Sci*. **2007**, *601*, 1590–1598.

[34] Govindasamy, G.; Murugasen, P.; Sagadevan, S. Optical and electrical properties of chemical bath deposited cobalt sulphide thin films. *Mater. Res*. **2017**, *20*, 62–67.

[35] Wang, Y. Q.; Zou, Y. Q.; Tao, L.; Wang, Y. Y.; Huang, G.; Du, S. Q.; Wang, S. Y. Rational design of three-phase interfaces for electrocatalysis. *Nano Res*. **2019**, *12*, 2055–2066.